BAT AGN Spectroscopic Survey – XIX. Type 1 versus type 2 AGN dichotomy from the point of view of ionized outflows

A. F. Rojas [1,2]★ E. Sani,[1] I. Gavignaud,[2] C. Ricci [3,4] I. Lamperti,[5] M. Koss [6]
B. Trakhtenbrot [7] K. Schawinski,[8] K. Oh,[9,10] F. E. Bauer,[11,12,13] M. Bischetti,[14]
R. Boissay-Malaquin,[15] A. Bongiorno,[14] F. Harrison,[16] D. Kakkad,[1] N. Masetti,[2,17]
F. Ricci [11] T. Shimizu [18] M. Stalevski [19,20] D. Stern[21] and G. Vietri[22,23,24]

Affiliations are listed at the end of the paper

ABSTRACT

We present a detailed study of ionized outflows in a large sample of ∼650 hard X-ray-detected active galactic neuclei (AGNs). Using optical spectroscopy from the BAT AGN Spectroscopic Survey (BASS), we are able to reveal the faint wings of the [O III] emission lines associated with outflows covering, for the first time, an unexplored range of low AGN bolometric luminosity at low redshift ($z \sim 0.05$). We test if and how the incidence and velocity of ionized outflow is related to AGN physical parameters: black hole mass (M_{BH}), gas column density (N_H), Eddington ratio (λ_{Edd}), [O III], X-ray, and bolometric luminosities. We find a higher occurrence of ionized outflows in type 1.9 (55 per cent) and type 1 AGNs (46 per cent) with respect to type 2 AGNs (24 per cent). While outflows in type 2 AGNs are evenly balanced between blue and red velocity offsets with respect to the [O III] narrow component, they are almost exclusively blueshifted in type 1 and type 1.9 AGNs. We observe a significant dependence between the outflow occurrence and accretion rate, which becomes relevant at high Eddington ratios [$\log(\lambda_{Edd}) \gtrsim -1.7$]. We interpret such behaviour in the framework of covering factor-Eddington ratio dependence. We do not find strong trends of the outflow maximum velocity with AGN physical parameters, as an increase with bolometric luminosity can be only identified when including samples of AGNs at high luminosity and high redshift taken from literature.

Key words: galaxies: active – galaxies: nuclei – quasars: emission lines.

1 INTRODUCTION

A direct link between galaxy formation and the growth of the central supermassive black hole (SMBH) was found almost 20 yr ago with the discovery of black hole (BH) mass–bulge scaling relations (e.g. Ferrarese & Merritt 2000; Gebhardt et al. 2000; Sani et al. 2011; Kormendy & Ho 2013). The underlying mechanism linking the two processes is thought to be active galactic nucleus (AGN) feedback, i.e. the release of energy by the AGN into the interstellar medium (ISM). Theoretical models have proposed that AGN feedback regulates star formation (SF) by removing and/or heating the gas, so that a star-forming galaxy evolves into a red early-type galaxy (e.g. Granato et al. 2004; Di Matteo, Springel & Hernquist 2005; Hopkins et al. 2006; Merloni & Heinz 2008). The majority of AGN feedback is thought to come in two flavours, at low Eddington ratios

radio-jets dominate kinetic feedback (e.g. Fabian 2012) whereas at higher Eddington ratios radiation pressure from the accretion disc is responsible for gas outflows. In a considerable fraction of AGNs, there are signatures of outflows capable of removing significant amounts of cold gas from the host galaxy (Feruglio et al. 2010, 2015; Rupke & Veilleux 2013; Cicone et al. 2014) or heating the gas (e.g. Shangguan, Ho & Xie 2018). None the less, studies exploring the role of AGNs with respect to SF have led to ambiguous results, not finding any compelling evidence of negative feedback (Balmaverde et al. 2016) and even evidence of positive feedback, with outflows generating local SF (Ishibashi & Fabian 2012; Cresci et al. 2015; Maiolino et al. 2017). Additionally, some authors showed that the observed SMBH–host scaling relations can be reproduced without invoking feedback mechanisms, simply as a result of the hierarchical assembly of BHs and stellar mass through galaxy merging (e.g. Peng 2007; Hirschmann et al. 2010; Jahnke & Macciò 2011).

High-velocity (>1000 km s^{-1}) and extended AGN-driven outflows are frequently detected in local and high-redshift galaxies,

at different luminosities, in ionized, neutral, and molecular gas. In particular, high-resolution, integral field spectroscopic observations and millimetre interferometers have revealed the presence of ionized and molecular gas outflows, respectively, with high velocities, >1000 km s^{-1}, in low- and high-redshift galaxies, and can allow the characterization of their outflow properties, such as the extension of the ejected material as well as the entrained masses and associated energy (Harrison et al. 2012, 2014, 2016; Cicone et al. 2014; Cresci et al. 2015; Perna et al. 2015a, b; Brusa et al. 2016; Carniani et al. 2016; Kakkad et al. 2016; Bischetti et al. 2017; Kang & Woo 2018).

Numerous efforts have been done to test the occurrence of ionized outflows, finding them in a large fraction of SDSS AGNs, from $\sim$20–40 per cent to $\sim$50–70 per cent depending on the AGN type (Véron-Cetty, Véron & Gonçalves 2001; Balmaverde et al. 2016; Harrison et al. 2016; Woo et al. 2016; Perna et al. 2017; Woo, Son & Bae 2017; Rakshit & Woo 2018).

However, most of the samples considered by these studies are incomplete due to biases against absorption in the optical/soft X-ray band. Therefore it has been difficult to place the outflow signatures of galaxy populations in the context of both obscured and unobscured AGNs. The physical processes responsible for the origin of outflows, their frequency within an unbiased sample of AGNs, and how they can affect the evolution of the host galaxy and its ISM are still open questions. Hard X-ray selection offers the least biased AGN selection (e.g. Baumgartner et al. 2013) thanks to the low contamination from other sources within the host galaxy and the high penetration ability of hard X-rays up to large gas column densities ($N_H \leq \sigma_T^{-1} \approx 1.5 \times 10^{24}$ cm^{-2}, where σ_T is the Thomson cross-section), see e.g. Ricci et al. (2015). The *BAT AGN Spectroscopic Survey* (BASS; Koss et al. 2017; Ricci et al. 2017a) allows us to take advantage of an unbiased local sample of $\sim$650 AGNs to study the occurrence of ionized outflows traced by the [O III] $\lambda\lambda$4959, 5007 emission lines and how they are related to other key AGN properties (bolometric luminosity L_{Bol}, Eddington ratio $\lambda_{Edd} = L_{Bol}/L_{Edd} \propto L_{Bol}/M_{BH}$, column density N_H, intrinsic L_X). The [O III] emission lines are frequently used to study outflows because they are a bright doublet in the optical range. They trace the gas ionized by the AGN at distances which are not affected by the gravitational potential of the central SMBH. Any broadening of these lines can be safely assumed to be due to gas kinematics in the narrow-line region (NLR).

Moreover, studies exploring the role of radiation pressure on the obscuring material lead to interesting results which can be tested with our study on the incidence of outflows. Ricci et al. (2017b) investigated the obscuration properties of the BASS sample and found that radiative feedback on dusty gas regulates the distribution of the obscuring material, such that SMBHs accreting with log(λ_{Edd}) > -1.5 have a lower covering factor ($\sim$40 per cent). This is likely due to the fact that radiation pressure is able to expel a large fraction of the dusty gas in the form of outflows.

The aim of our work is to test such a hypothesis by looking at the incidence of ionized outflows and how they relate, in terms of wind velocities, outflowing mass rate, and wind power, to the central SMBH and host galaxy parameters. The paper is structured as follows: in Section 2, we provide information about the sample selection; in Section 3, we describe the methods adopted to determine the outflows velocities from the optical spectra and fitting method used; in Section 4, we present the results derived from our multicomponent line fits to the [O III] λ5007 profiles; in Section 5, we discuss how the occurrence of outflows evolves as a function of parameters such as the Eddington ratio, [O III] λ5007 luminosity,

and spectral classification (i.e. optical type 1, type 2); finally, in Section 6 we summarize the main conclusions of our work. In the following, we assume a cosmology with $H_0 = 70$ km s^{-1} Mpc^{-1}, $\Omega_\Lambda = 0.7$, and $\Omega_m = 0.3$.

2 DATA

The Burst Alert Telescope (BAT) instrument onboard *Swift* satellite (Gehrels et al. 2004) is carrying out an all-sky survey in the ultra-hard X-ray band (>10 keV) that, as of the first 70 months of operation, identified 1210 objects (Baumgartner et al. 2013) of which 836 are classified as AGNs based on their associations with objects in the medium and soft energy X-ray band, and using NED and SIMBAD databases.

The optical spectral data used in this work are part of the BASS sample (Koss et al. 2017), a dedicated multiwavelength follow-up project for the nearby, powerful AGNs identified by *Swift*-BAT 70-month catalogue. BASS optical data release 1 (DR1, Koss et al. 2017)[1] compiled optical spectra of 642 AGNs, taken from public surveys such as SDSS or previously published papers (67 per cent, 433/642, e.g. Rojas et al. 2017; Masetti et al. 2013, and references therein), and from targeted campaigns (33 per cent, 209/642). DR1 presents redshift, classification, black hole mass (M_{BH}), bolometric luminosity (L_{Bol}), Eddington ratio (λ_{Edd}), and optical spectral properties such as emission line strengths and velocity dispersions for the majority of obscured and unobscured AGNs (74 per cent, 473/642), including 340 AGNs for which M_{BH} and λ_{Edd} are measured for the first time.

The BASS sample is nearly unbiased against obscuration up to Compton-thick levels ($N_H > 10^{24}$ cm^{-2}) due to its selection from the hard X-ray band (14–195 keV). Koss et al. (2017) presented an overview of the optical spectroscopic data. Additional extended multiwavelength campaigns from near-IR (NIR) to soft X-ray wavelengths (Berney et al. 2015; Lamperti et al. 2017; Oh et al. 2017; Ricci et al. 2017a, 2017b; Trakhtenbrot et al. 2017; Koss et al. 2018; Oh et al. 2018; Powell et al. 2018; Ricci et al. 2018; Shimizu et al. 2018; Baek et al. 2019; Bär et al. 2019; Ichikawa et al. 2019; Paliya et al. 2019) have allowed us to further characterize the BASS sample, studying for example the connection between X-ray and optical obscuration, NIR lines, X-ray photon index, absorption, and coronal properties.

2.1 Sample selection

Our main focus is to identify outflows, and therefore to spot the faint wings of the [O III] λ5007 emission line and test how asymmetric/broad profiles associated with ionized outflows relate to other key AGN properties. To provide reliable measurements, we excluded from the analysis cases where the [O III] emission is too faint to properly parametrize the wings or where the noise on the continuum is so high that it dilutes such wings. Therefore, we adopt a threshold in S/N to discard unreliable spectra, where the noise level was estimated by considering the dispersion of the continuum in the [O III] region, and the signal from the [O III] emission. From the 642 DR1 spectra, we exclude 59 sources with S/N < 7, and 36 spectra that do not cover the Hβ + [O III] region. In total, we consider 547 spectra of the whole sample (85 per cent of the BASS DR1 catalogue). After these cuts, our sample contains 210 type 2 (defined as AGNs with only narrow permitted and forbidden

---

[1]https://www.bass-survey.com

emission lines in the optical spectra, full width at half-maximum or FWHM $\leq$ 1000 km s^{-1}), 92 type 1.9 (defined as AGNs with only narrow emission lines aside from a broad profile of FWHM $\geq$ 1000 km s^{-1} seen from H α), and 245 'type 1' (defined as AGNs with broad permitted lines beyond H α plus narrower forbidden lines; note that we group together all Seyfert subtypes 1.0, 1.2, 1.5, and 1.8 here). For the following analysis, we adopt the AGN classification determined in Koss et al. (2017) by means of BPT (Baldwin, Phillips & Terlevich) diagnostic diagrams, depending on the presence and strength of broad emission lines, and the type 1 subtypes classification based on Winkler (1992).

3 SPECTRAL ANALYSIS

In order to identify outflow signatures in our sample, we use the profile of [O III] λ5007 emission lines in the rest-frame optical spectra.

These emission lines are produced through a forbidden transition and are only emitted by low-density gas ($n_H \leq 10^6$ cm^{-3}) located in the NLR, which is an extended region (1–1000 pc) of gas clouds photoionized by the non-stellar continuum emission of the AGN (Peterson 1997). The velocity dispersions of such clouds are intrinsically narrow (FWHM $\leq$ 1000 km s^{-1}) and therefore any broadening or shifting of the [O III] emission lines is interpreted as the result of outflowing gas in the NLR, which can be extended over kpc scales (e.g. Pogge 1989), as opposed to the more dense, sub-pc-sized broad-line region (BLR).

The emission-line profiles of ionized gas in AGN host galaxies often appear to be non-Gaussian and asymmetric, composed of a narrow (systemic) component plus a wing. In addition, the line centroids are often blueshifted (or redshifted) relative to the systemic velocity of the host galaxy, as measured by the stellar light. Such asymmetries are usually interpreted as a result of outflowing gas in the NLR. The effect tends to be stronger in the higher ionization lines (Veilleux 1991), and thus we focus our attention on the [O III] $\lambda\lambda$4959, 5007 doublet, and in particular on the [O III] λ5007 emission line.

In this section we describe the procedure used to model the profile of the H β + [O III] spectral region (4400–5500 Å).

3.1 Continuum fitting (4400–5500 Å)

To model the inner regions of the AGN and obtain the parameters characterizing the gas kinematics, we adopt a multicomponent spectral fit using PYSPECKIT, an extensive spectroscopic analysis toolkit for astronomy, which uses a Levenberg–Marquardt minimization algorithm (Ginsburg & Mirocha 2011).

Prior to the multicomponent fitting of the emission lines, we first removed the underlying AGN continuum or the host galaxy emission. A pseudo-continuum slope is define by two narrow (10 Å) emission-line free regions [4440–4450 or 4720–4730 Å, and 5110–5120 Å; see Shen et al. (2016)]. Depending on the AGN spectral type and complexity, we additionally used a Fe II grid of templates or stellar population synthesis models to fit the underlying continuum (see below for details). The best-fitting template is chosen by minimizing the χ^2, and it is then subtracted from the spectra so that the pseudo-continuum made by the Fe II emission can be measured to fit the emission lines.

A major complication in fitting type 1 AGN spectra is that the complex Fe II emission lines contaminate almost entirely the 4400–5500 Å waveband including the [O III] profile. We used both empirical and synthetic Fe II templates to fit the iron emission (Boroson &

Table 1. Parameters of the Fe II simulated templates for different physical conditions of the BLR. Each column indicates a template, with the ionized photon flux emitted by the primary source [Φ(H)] and electron density in the BLR clouds (n_e) used as input for CLOUDY. For these conditions, we consider the case with a microturbulence velocity and the case without that velocity.

$\log\left(\frac{\Phi(\mathrm{H})}{\mathrm{cm}^{-2}\,\mathrm{s}^{-1}}\right)$:	17	17	19	17	19	21	17	19	21	23
$\log\left(\frac{n_e}{\mathrm{cm}^{-3}}\right)$:	8	10	10	12	12	12	14	14	14	14

Green 1992; Bischetti et al. 2017; Vietri et al. 2018). However, we were not able to obtain a satisfactory fit to the Fe II emission using the empirical ones because the [O III] emission lines in their spectra are blended with the iron features thus producing artificial outflow signals. Therefore, we considered 20 synthetic models to account for the Fe II emission in the H β + [O III] region and clean our type 1 AGN sample of that emission. The templates were created by the photoionization simulation code CLOUDY (Ferland et al. 2013), for different ionizing photon fluxes emitted by the primary source [Φ(H)] and electron densities in the BLR clouds (n_e), with and without the possibility of a microturbulence velocity ($u_{turb} = 0$ or 100 km s^{-1}). The parameters for each Fe II model are listed in Table 1. Each template is then convolved with a set of Gaussian profiles of increasing width from 1200 to 20 000 km s^{-1} in steps of 25 km s^{-1}. We refer hereafter to the resulting broadened templates as 'sub-templates'.

The continuum fitting procedure applied to each type 1 AGN spectrum is as follows:

– A linear pseudo-continuum is fitted within the spectral windows 5110–5120 and 4400–4450 Å (or 4720–4730 Å) and subtracted from the spectrum.

– For each AGN spectrum, a best-fitting Fe II sub-template is selected from each of the 20 original synthetic models, restricting the broadening width to be within 2000 Å of the FWHM of H β, that is generally what we observed (table 9 of the BASS DR1; Koss et al. 2017). The Fe II sub-templates are normalized considering the AGN spectrum within the 4450–4750 and 5050–5400 Å windows. The selected sub-template is the one which minimizes the residuals in the 4450–4650 and 5100–5400 Å spectral regions where the iron emission is usually strongest.

– Finally, we select the normalized best-fitting Fe II sub-template with the lowest residuals from the type 1 AGN spectra. Our final sample with a satisfactory continuum and Fe II template subtraction totals 167 type 1 AGNs.

In the case of type 2 and 1.9 AGNs, the major contamination in the spectra is the stellar component. A large set of single stellar population synthesis templates was used to model and subtract the host stellar component from each galaxy spectrum using the penalized PiXel Fitting software (PPXF; Cappellari & Emsellem 2004). The templates used are from the Miles Indo-U.S. Catalog (MIUSCAT) library of stellar spectra (Vazdekis et al. 2012). The galaxy continuum and stellar absorption features were removed, as explained in Koss et al. (2017) and in Lamperti et al. (2017). Our final sample is comprised of 210 type 2 AGNs and 92 type 1.9 AGNs with a satisfactory host continuum subtraction.

Finally, depending on the spectral type and gas kinematics, the emission lines are modelled by means of multi-Gaussian components (narrow, broad, and outflow) in the continuum and Fe II subtracted spectra for type 1 AGNs or the host continuum-subtracted spectra of type 2 and type 1.9 AGNs, respectively.

3.2 Multicomponent line fitting (4400–5500 Å)

3.2.1 Seyfert 1.9 and Seyfert 2 AGNs

We fit a linear (pseudo-)continuum based on continuum windows (4660–4670, 4700–4750, and 5040–5200 Å). Seyfert 1.9 AGNs are characterized by a broad component detected in Hα but not Hβ; therefore we describe the emission line fitting of Seyfert 1.9 and 2 AGNs together. We fit narrow components for the He II λ4686, Hβ and [O III] $\lambda\lambda$4959, 5007 emission lines, and we consider an additional broad outflowing (offset) component for Hβ and for each [O III] line in order to distinguish outflow signatures. We note that a single-Gaussian fit (i.e. one per emission line) often fails to account for the complex emission-line profiles seen in many BASS AGNs, and a second broad component fit to the [O III] lines allows us to find and characterize asymmetric profiles.

We tied together the rest-frame centroids of the narrow components of the emission lines ($\lambda_{\text{He II}}=\lambda_{\text{H}\beta}-175$ Å; $\lambda_{\text{H}\beta}=\lambda_{\text{[O III]}5007}-146$ Å; $\lambda_{\text{[O III]}4959}=\lambda_{\text{[O III]}5007}-48$ Å) and the broad components of the lines were tied together in order to identify their blue- or redshift common to all these lines.

We allow for velocity offsets of up to ±600 km s^{-1} in the narrow component and ±1800 km s^{-1} in the broad components, compared to the database redshift. Such large velocity shifts are motivated by the observations of a mean velocity shift of the broad Hβ to the systemic redshift of 109 km s^{-1} with a scatter of 400 km s^{-1} in a sample of 849 quasars (Shen et al. 2016).

The widths of the narrow lines are also tied together [$\sigma_{\text{H}\beta}$ (narrow) $= \sigma_{\text{[O III]}5007}$ (narrow) $= \sigma_{\text{[O III]}4959}$ (narrow)], with an initial input guess of $\sigma_{\text{narrow}} = 300$ km s^{-1} (~5 Å). We constrain the FWHM of the narrow lines to be less than 1200 km s^{-1} in all cases. Likewise, we tied together the widths of the broad components [$\sigma_{\text{H}\beta}$ (broad) $= \sigma_{\text{[O III]}5007}$ (broad) $= \sigma_{\text{[O III]}4959}$ (broad)] and set an initial value of $\sigma_{\text{broad}} = 500$ km s^{-1} (~8 Å) with no upper limit.

For an initial estimate of the amplitudes of the narrow lines, we measured the maximum value of the (continuum-subtracted) flux density in the region where the line is supposed to be (±5 Å of theoretical wavelength), and used that value as the initial guess. For the amplitude of the broad components, we used 50 per cent of the maximum value as the initial guess. Additionally, we fixed the intensities of [O III] λ4959 and [O III] λ5007 to the theoretical ratio 1:2.86 for both broad and narrow components of the [O III] doublet, according to atomic physics (Storey & Zeippen 2000; Dimitrijević et al. 2007).

3.2.2 Seyfert 1 AGNs

After the continuum and Fe II emission have been subtracted, we consider two velocity components (narrow + broad) for each line in the region: He II λ4686, Hβ λ4861, [O III] $\lambda\lambda$4959, 5007, adopting the same initial guesses for amplitudes, wavelengths, and widths used for type 2 and type 1.9 AGNs. But in these AGNs, we consider an additional broad component of Hβ to account for the BLR emission. Therefore, we have three components for Hβ, one narrow component, one broad component for the outflow, and a very broad BLR component. The first broad component is modelled using the same initial guesses as for type 2 AGNs in order to model a possible outflow component, while the second broad component is left free in wavelength and width because we do not know the characteristics of the BLR for each AGN. In Fig. 1, we show two examples of spectra illustrating our fitting method.

3.2.3 Errors estimation

For all the sources, we estimated the errors associated with each fitted parameter using Monte Carlo simulations. We repeated the entire fitting procedure (including line emission components and continuum) 100 times, each time adding an amount of noise to each spectral bin randomly drawn from a normal distribution based on the standard deviation of the corresponding local continuum level of each spectrum. From these, we computed the standard deviation of the mean of the 100 measurements and used this value as an estimate of the error at the 1σ confidence level. We performed a visual inspection of all the emission line fits to verify proper fitting. We stress that with this method we can address any kind of uncertainties, included those related to the continuum fitting to which low-amplitude broad-line components can be highly sensitive.

4 RESULTS

Here we describe the strategy to detect outflows in the BASS DR1 sample and their incidence. Outflow velocities and related properties were estimated from the [O III] λ5007 emission lines adopting well-known parametric and non-parametric prescriptions, as presented below. These two prescriptions serve as consistency checks and allow us to properly compare our results with various literature samples (e.g. Alexander & Hickox 2012; Harrison et al. 2014).

4.1 Detection of ionized outflows

We used the fitted parameters of the two components of [O III] λ5007 emission line (narrow and broad) to define an outflow detection and corresponding velocity.

A non-Gaussian profile in the [O III] emission lines, with relatively stronger wings/tails than a Gaussian, is indicative of an ionized wind. The profiles usually show a blue (or occasionally red) wing, i.e. the profile of the lines is reproduced with two components, a narrow one associated with the emission from the NLR and the second broad component that can be shifted. In this work this second component is considered to be an outflow candidate.

To consider a secondary broad component as reliable, we imposed a detection limit of 3σ, based on the standard deviation of the baseline fitting without emission lines. Since most line profiles are found to be asymmetric (Perna et al. 2017), we consider a blue or redshifted outflow detection when the wavelength shift between the two components of [O III] line is significant compared to the errors.

We define the wavelength shift between the broad component that represents the outflow and the narrow component of the line as

$$\Delta\lambda = \lambda_{\text{[O III]},\text{Narrow}} - \lambda_{\text{[O III]},\text{Broad}}. \qquad (1)$$

A blueshifted outflow arises when $\Delta\lambda > \epsilon_\lambda$ and a redshifted outflow when $\Delta\lambda < -\epsilon_\lambda$, where $\epsilon_\lambda = \sqrt{(\epsilon_{\text{broad}}^2 + \epsilon_{\text{narrow}}^2)}$ with ϵ_{broad} and ϵ_{narrow} being the fitting errors on the central wavelengths of both components.

Finally, the maximum outflow velocity was estimated following the approach of Rupke & Veilleux (2013), assuming that the outflow expands with constant velocity:

$$v_{\text{max}} = \Delta\lambda + 2\sigma_{\text{[O III]},\text{Broad}}, \qquad (2)$$

where $\sigma_{\text{[O III]},\text{Broad}}$ is the velocity dispersion parameter of the Gaussian representing the broad component of the [O III] line.

In order to avoid biases associated with the outflow detection criteria assumed, we also adopt a non-parametric velocity estimator
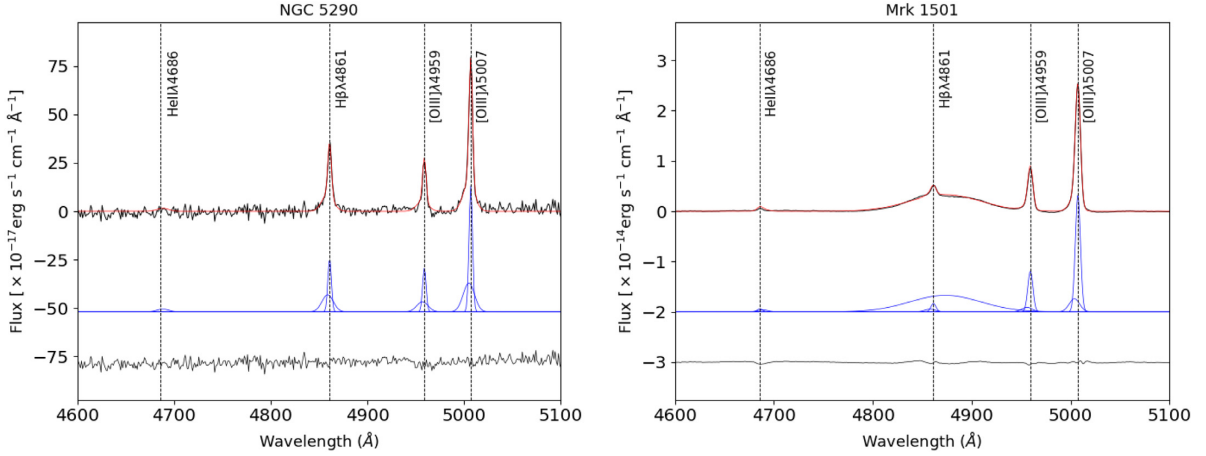
Figure 1. Examples of our fitting method. *Left*: An example of type 2 AGNs fitting after stellar component subtraction. *Right*: Spectral fitting of a type 1 AGN after continuum and Fe II subtraction. For each object, we show the spectra (in black), the components fitted for emission lines (in blue), the overall best-fitting model (in red), and the residuals below. The dashed vertical lines mark the location of He II λ4686, Hβ λ4861, and [O III] λλ4959, 5007.
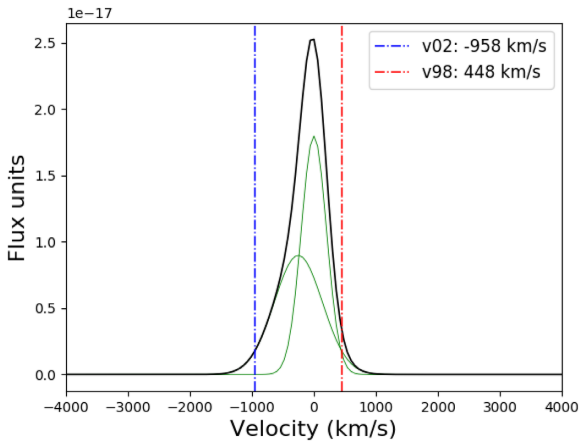
Figure 2. Example of [O III] emission-line reconstruction from the narrow and broad components obtained after fitting 100 Monte Carlo simulations. The non-parametric 98th (v98) and 2nd (v02) velocity percentiles are shown as vertical dashed lines, while their values are quoted with respect to the narrow centroid as 0 km s^{-1} in the legend; the larger of the absolute values of v02 and v98 is considered v$_{max}$ (in this case v02).

frequently used in literature (see e.g. Harrison et al. 2014; Zakamska & Greene 2014; Balmaverde et al. 2016; Perna et al. 2017) to estimate the outflow properties from the [O III] emission line. To start, we reconstruct a synthetic line profile for [O III] λ5007 using the average of the best-fitting parameters from in the 100 Monte Carlo simulations discussed in Section 3.2. Then, we measure the velocity at which a given fraction of the line flux is collected using the cumulative flux function $F(v) = \int_{-\infty}^{v} F_v(v') dv'$ and defining differentpercentiles of the overall line flux (v02, v05, v50, etc.). An example can be found in Fig. 2.

The degree of line asymmetry is estimated by the dimensionless *R* parameter introduced by Zakamska & Greene (2014):

$$R = \frac{(v95 - v50) - (v50 - v05)}{(v95 - v05)}. \quad (3)$$

When $R < 0$, a blue prominent broad wing is present and the maximum outflow velocity v$_{max}$ is defined as v02. When $R > 0$, a red wing is present and the v_{max} corresponds to v98. The velocity offset of the broad wing is defined as $\Delta v = \frac{(v05 + v95)}{2}$ and the velocity

shift respect to the velocity peak ($v_p = v50$) of the whole line is given by $|\Delta v| - v_p$.

Once we have the velocities, following Perna et al. (2017), we consider a velocity threshold of $v_{max} = 650$ km s^{-1} to discriminate between kinematics dominated by gravitational broadening and outflow processes. This criterion is applied to the maximum velocities estimated from both the parametric and non-parametric methods. Once applied, we find consistency between the methods for the majority (65 per cent) of the AGN with outflow signals detected.

Overall, we considered an outflow signal to be firmly detected if the asymmetry is found by both methods. In case the outflow was found with only one method, we visually inspected the line profile to decide whether the outflows was detected reliably or not.

For the visual check, we also considered the possibility to have symmetric outflows, i.e. where the second broad component of [O III] λ5007 is necessary to reproduce the line profile, but has no considerable wavelength shift with respect to the narrow component. With this approach we found 19 additional blueshifted, 6 redshifted outflows, and 6 with signals of a symmetric outflow for type 1 AGNs. For type 1.9, we found nine additional blueshifted outflows, three additional redshifted outflows, and two AGNs with symmetric outflow. Finally, for type 2 AGNs, we found 11 additional blueshifted outflows, 6 redshifted and 3 with symmetric outflow after visual inspection.

In the following, we adopt the maximum velocities of outflows estimated from the parametric method (equation 2). We show in Fig. 3 a comparison between the maximum outflow velocities estimated by each method. We can see that most of the data points lie systematically below the 1:1 ratio line, with higher velocities showing a more consistent deviation. This behaviour, whereby the parametric method estimates larger velocities than the non-parametric method, is expected since the parametric method uses the parameters representing the outflowing gas, while the non-parametric method estimates the velocities from the whole [O III] emission line (v02, v098), and thus its maximum velocity can be strong down-weighted by the narrow-line emission.

4.2 Outflow statistics

Based on the analysis described above, we detect outflows in all AGN types, spanning a broad range in luminosity and SMBH mass
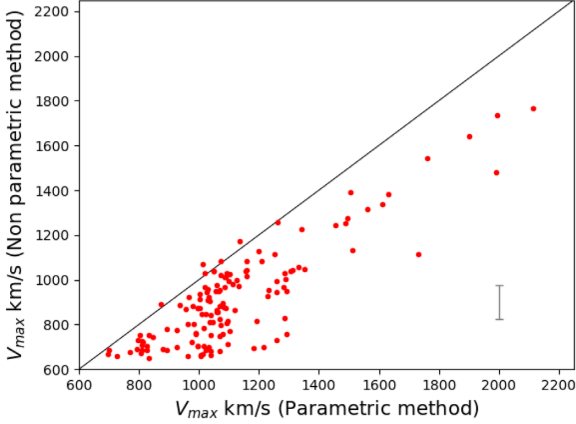
Figure 3. Comparison between maximum outflow velocities estimated using the two detection methods, parametric (*x*-axis), and non-parametric (*y*-axis). A typical error bar ($\pm 150\,\mathrm{km\,s^{-1}}$) is shown for reference.
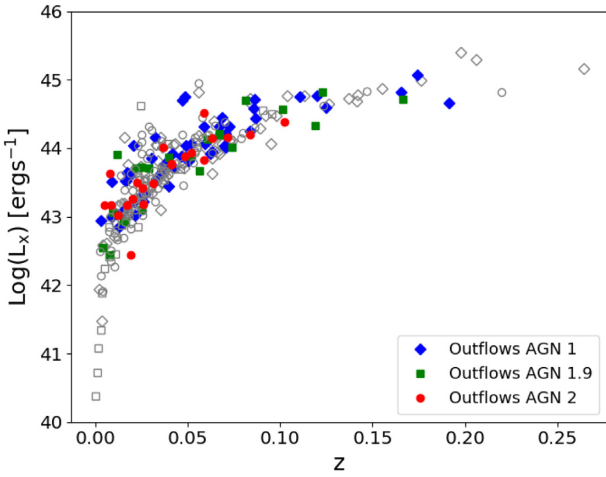

Figure 4. X-ray luminosity (14–195 keV) as a function of redshift for our sample, with symbols distinguishing: AGN 1 (diamonds), AGN 1.9 (squares), and AGN 2 (circles). Open grey symbols indicate AGNs with no measurable outflow signal for the different types, while filled, colour-coded symbols denote AGNs with outflows detected as described in Section 4.1.

up to $z \sim 0.2$ (see Figs 4 and 5). Overall, 38 ± 2 per cent of the BASS sample analysed (178/469) exhibit detectable ionized outflows signatures, with 29 per cent showing blueshifted and 7 per cent redshifted.

We found that: 46 ± 4 per cent of type 1 AGNs have signals of outflows, mostly blueshifted; 55 ± 5 per cent of type 1.9 AGNs have outflows detections, also mostly blueshifted; and 24 ± 3 per cent of type 2 AGNs have signals of outflows, but with comparable fractions being blueshifted and redshifted.

In Fig. 4, we show AGNs with outflow signals with colour-coded symbols compared with AGNs without outflows (open grey symbols). We find that AGNs with detected outflows span X-ray luminosities between 10^{42} and 10^{46} erg s^{-1} for the different subtypes. Independent of AGN type, we do not find outflows for AGNs with $L_X < 3 \times 10^{42}$ erg s^{-1}, implying that these AGNs may not be powerful enough to drive strong outflows and/or the wings of the [O III] lines are too faint to be detected. We also note that among the few high-luminosity AGNs found with outflows at $z \gtrsim 0.1$, the type 2 AGN fraction is quite low (1/4). Clearly the results
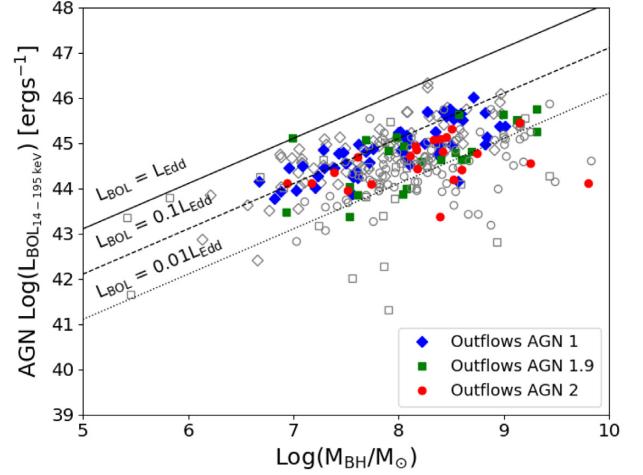
Figure 5. Bolometric luminosity as a function of SMBH mass for our sample. Symbols are identical to Fig. 4. The lines correspond to $L_{\mathrm{Bol}} = L_{\mathrm{Edd}}$ (solid), $L_{\mathrm{Bol}} = 0.1L_{\mathrm{Edd}}$ (dashed), and $L_{\mathrm{Bol}} = 0.01L_{\mathrm{Edd}}$ (dotted).

suffer from poor statistics, but may also arise from a dilution effect caused by the host galaxy; for a given slit width, the farther the system is, the larger is the contribution of the host galaxy entering in the slit, thus diluting a possible wind signature. Given the small number of distant sources, this potential bias anyhow does not affect our results.

Fig. 5 shows the bolometric luminosity as a function of M_{BH} for the AGN with outflow signals (colour-coded symbols) compared with AGNs without outflows (open grey symbols) in our sample. The BASS sample criteria selects a wide range of bolometric luminosities ($\sim 10^{42}$–10^{46} erg s^{-1}) and BH masses ($\sim 10^{7}$–10^{10} M$_\odot$). The lines correspond to different accretion efficiencies commonly used in the literature to estimate the fraction of AGN bolometric luminosity in the form of the outflow power. Eddington luminosities L_{Edd} correspond to: $1.26 \times 10^{38}(M_{\mathrm{BH}}/M_\odot)$ erg s^{-1}. The distribution of AGNs with outflows in the L_{Bol}–M_{BH} plane spans a comparable range as the full BASS sample. We can see that the detected outflows generally reside at slightly higher $L_{\mathrm{Bol}}/L_{\mathrm{Edd}}$ values than non-detections. This might be either due to low efficiency of the AGN engine in driving the wind, or due to the faintness of the wings in the [O III] line. We note however that the cut applied in S/N should mitigate this last effect. Specifically, type 1 AGNs with outflows signatures are preferentially located at high Eddington ratios than type 1.9 and 2 (see Section 5.4 for more details).

The statistics of the detected outflows are shown in Fig. 6 for the different AGN types, where top panels indicate the wavelength shift between the narrow and broad component of the [O III] line ($\Delta\lambda$), i.e. the measured asymmetry of the line that represents the outflow itself, and the bottom panels indicate maximum outflow velocities from the geometrical models assumed and discussed below.

5 DISCUSSION

In this section, we propose a geometrical interpretation of the results obtained in Section 4, we then present the mass rate and kinetic power of the outflows of BASS AGNs, and finally, we test the outflow fraction as a function of different AGN power tracers.
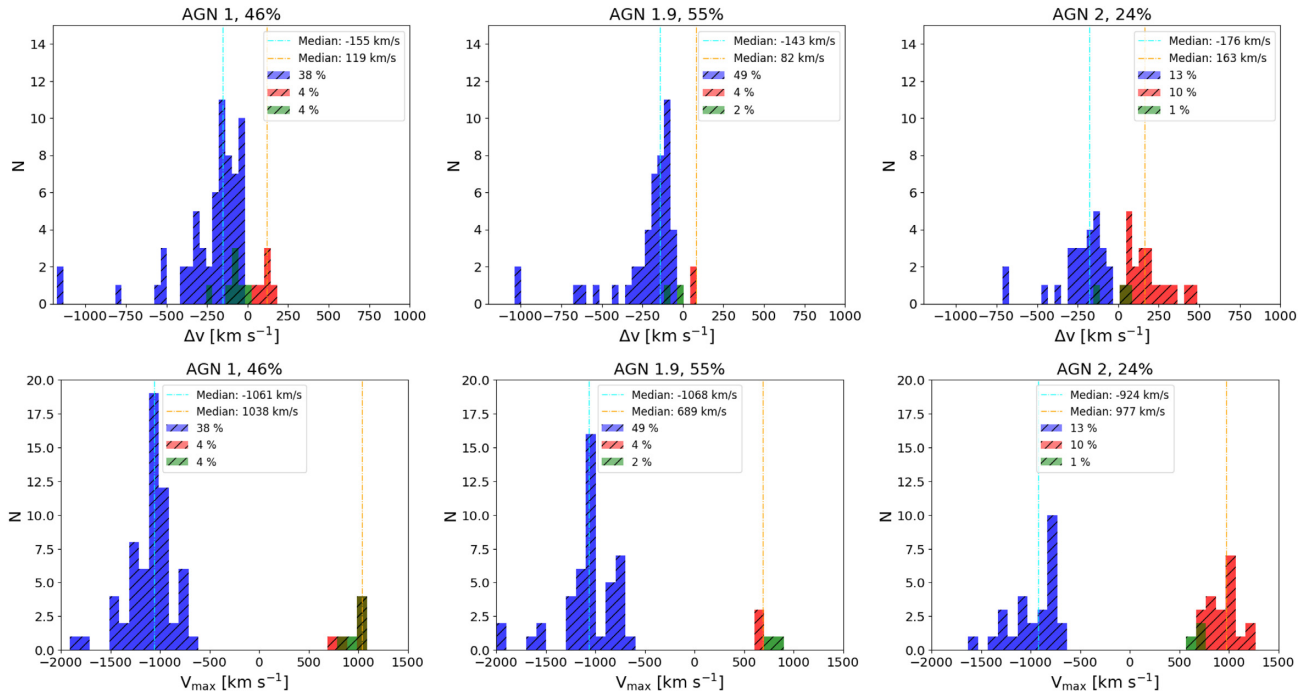
Figure 6. Distributions of sources with ionized outflows as a function of wavelength shift (top) and maximum velocity (bottom). The panels show wavelength shifts and velocity distribution for approaching, receding and symmetric outflows, represented with blue, red, and green histograms, respectively, for the subsamples defined on the basis of the AGN type. For each panel, the fraction of AGNs with outflow is indicated, together with the fraction of receding, approaching and symmetric outflows.

5.1 Outflow fraction

From the results presented in Fig. 6, we observe a clear disparity between type 1/type 1.9 and type 2 AGNs:

– The occurrence of outflow detections in type 1/type 1.9 AGNs is twice the one found in type 2 AGNs (i.e. 46 per cent and 55 per cent versus 24 per cent);

– Type 1 and type 1.9 AGN outflows are almost exclusively blueshifted, while type 2 AGNs exhibit a statistically equal number of redshifted and blueshifted outflows.

We interpret this latter difference in the framework of the geometrical unification model of AGNs (Antonucci 1993; Urry & Padovani 1995): for type 1–1.9 AGNs we only observe the outflow on the nearside (pointed towards us) because the redshifted outflowing material is obscured for a large range of orientations between the NLR and the host galaxy disc (Fischer et al. 2013) and/or the dusty torus, whereas for more edge-on AGNs, i.e. type 2 AGNs, we are able to see receding (redshifted) outflows in almost equal probability to blueshifted ones.

In the following analysis, type 1.9 and type 1 are grouped. For that, we tested if type 1.9 can be considered a subcategory of type 1 or they have most probably a nature of type 2 AGNs. For details, see Section 5.1.1.

Our findings are in qualitative agreement with the results presented by Rakshit & Woo (2018) for a large sample of low-redshift AGNs selected from the SDSS DR12 catalogue ($z < 0.3$), where blueshifted [O III] outflows are more frequently detected than redshifted ones by a factor of 3.6 in type 1 AGNs, while the ratio between blueshifted and redshifted [O III] is only 1.08 for type 2 AGNs due to projection and orientation effects. Overall, the outflow fractions found by Rakshit & Woo (2018) are larger than the fractions we find here for all AGN types. This is most likely

due to the identification and limits imposed by the different outflow detection methods, as well as the inherent [O III] luminosity of the different samples. In particular, our thresholds to distinguish winds from gravitational kinematics make our outflow selection criterion more restrictive, in line with the lower fractions found.

Perna et al. (2017) selected a sample that includes both type 1 and type 2 AGNs by cross-matching 2–10 keV detections from archival *XMM–Newton* and *Chandra* data with the SDSS DR12, and adopting the non-parametric method described in Section 4.1. We find similar outflow fractions for the various AGN types as Perna et al. (2017). If we further split the fraction of outflows by velocity shift, we find comparable fractions of blue and redshifted outflows in type 1 AGNs, while redshifted outflows are more frequently detected in our work by a factor of 8.

Since the main difference between our sample and that of Perna et al. (2017) is the selection in the harder (14–195 keV) versus softer (2–10 keV) X-ray band, respectively, we wanted to test whether redshifted outflows tend to be at larger N_{H} and therefore could be underrepresented in their sample. Fig. 7 shows that for type 2 AGNs, blueshifted and redshifted outflows populate the same range of N_{H}. The probability that the two subsamples come from two distinct families is negligible, with a Kolmogorov–Smirnov test value of 0.52 and p-value $= 0.07$.

In the following subsections, we study how the fraction of outflows is affected (or not) by different AGN properties.

5.1.1 Type 2 versus type 1.9 AGNs

Regarding the fraction of outflow detections in type 1/type 1.9 AGNs versus type 2 AGNs, there are a couple of factors that may contribute to the different percentages: (a) type 2 AGNs may include a population of extremely obscured objects, whereby an outflow
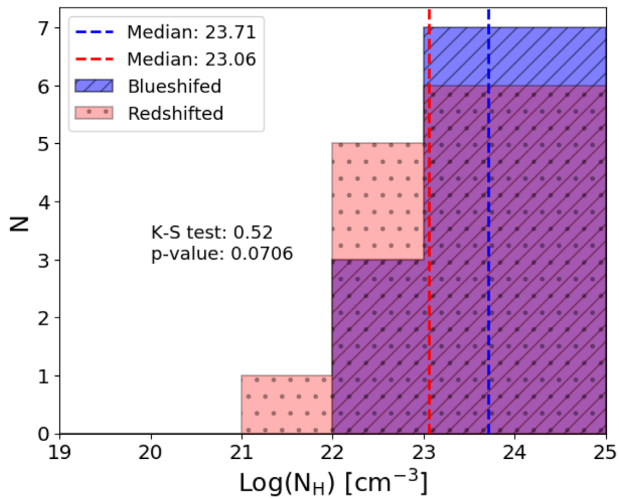
Figure 7. Log($N_{\rm H}$) comparing blueshifted and redshifted outflows in type 2 AGNs in fixed bins of column density.

has not yet managed to punch through the obscuring material; (b) Type 2 AGNs, on average, will have higher covering factors of the obscuring material around them. Thus, even though they might have intrinsically high $L_{\rm Bol}$ values, most of this luminosity will be reprocessed on small scales, and only a smaller fraction of that energy will be deposited into and drive ionized outflows.

Our results strengthen the hypothesis that type 1.9 AGNs should be considered as a sub-category of type 1 AGNs (e.g. Hernández-García et al. 2017 and references therein). In the following analysis we systematically find that type 1.9 and type 1 AGNs show similar behaviours, and for this reason we merge these two samples when presenting some results.

We have also considered the opposite view, i.e. that type 1.9 behave as type 2 Seyfert AGNs, where the BLR is mimicked in long-slit spectra by an outflow that broadens the emission lines [Shimizu et al. (2018); hereafter S18]. Of the 57 type 1.9 sources analysed in S18, 16 (28 per cent) are found to possibly be type 2 AGNs with the BLR simulated by an outflow that is detected in [O III]. We cross-checked our outflow detections with the BASS DR1 sub-sample studied in S18, and found that, in 14 type 1.9 AGNs over 16 sources

an outflow is detected based on our criteria. More specifically, we identify 11 blueshifted, 2 redshifted, and a symmetric outflow. As an exercise, we moved these 14 type 1.9 AGNs to the type 2 sub-sample. None of our results are significantly affected by this source redistribution. For example, the outflow fraction of type 2 AGNs increases from 24 per cent to 29 per cent, split into 17 per cent approaching and 11 per cent receding outflows.

5.2 Outflows fraction and gas column density

Theoretical models in which AGN activity is triggered by galaxy mergers propose an evolutionary path whereby obscured AGNs reside in star-forming galaxies during a period of rapid SMBH and galaxy growth, followed by a period where the AGN drives outflows that expel the surrounding material and reveal an unobscured AGN (e.g. Hopkins et al. 2006, 2008). As argued by past studies (e.g. Harrison et al. 2016), under this scenario we might expect a larger outflow fraction among the most X-ray obscured AGNs [log($N_{\rm H}$) > 22 cm^{-2}]. Using the column density ($N_{\rm H}$) estimated from X-ray spectral analysis of Ricci et al. (2017a) we observe the opposite trend (see Fig. 8, left-hand panel). In addition, Fig. 9 shows that higher velocities are not associated with the most obscured sources, where the data are dispersed and do not correlate significantly according to the Pearson test and Spearman rank (p-value = 0.05, R^2 = 0.04, and p-value = 0.01, ρ = $-$ 0.27, respectively). This is consistent with past findings (e.g. Harrison et al. 2016). At log ($N_{\rm H}$) < 21 cm^{-2}, indeed the fraction of detected outflows is almost two times higher than in more absorbed sources (a 2σ difference). However, projection effects might result in underestimated velocities for type 2 AGNs relative to type 1. Furthermore, contamination from the host galaxy might prevent the measurement of the highest velocities, which correspond to the faintest wings of the [O III] line profiles. Our results are in agreement with the analysis of Harrison et al. (2016), who analysed a sample of hard X-ray-selected AGNs at 0.6 < z < 1.7. To this end, we first highlight the left-hand panel of Fig. 8, where a clear anticorrelation between of the outflow fraction and $N_{\rm H}$ can be seen. The right-hand panel of Fig. 8 disentangles the evolution of type 1 + 1.9 and type 2 AGNs, demonstrating that the outflow fractions for type 1 and type 1.9 actually increase with $N_{\rm H}$. For type 2 AGNs, we observe the opposite trend, but with lower significance. We note that this type 1 + 1.9 AGNs trend in Fig. 8
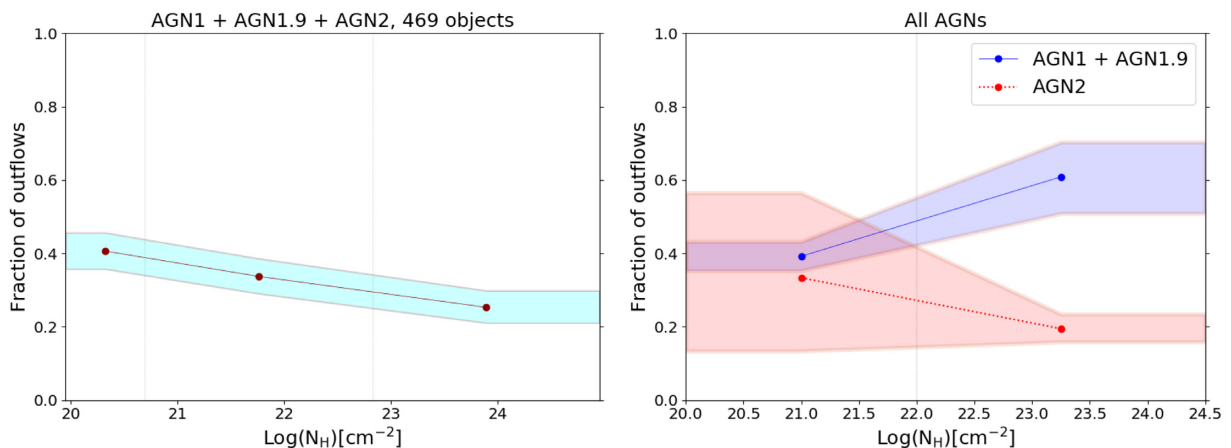

Figure 8. Left-hand panel: Fraction of outflows for different bins of log ($N_{\rm H}$) for the full sample. Bins are chosen to have the same number of objects and are indicated with grey vertical lines. Right-hand panel: Fraction of outflows for two different fixed bins of log ($N_{\rm H}$) comparing broad-line AGNs (AGN1 + AGN1.9, in cyan) and narrow-line AGNs (AGN2, in pink). The shaded area represents the 16th and 84th quantiles of a binomial distribution.
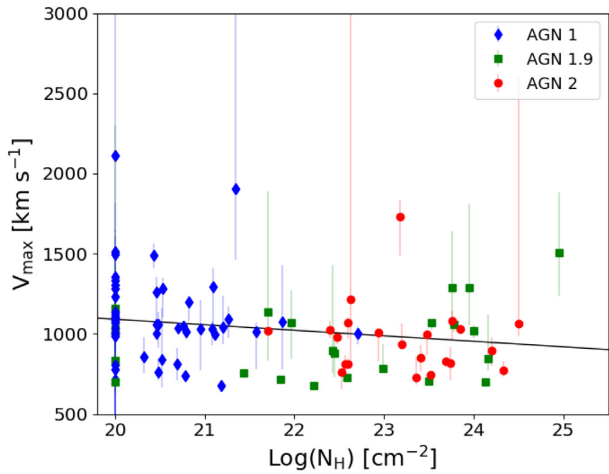
Figure 9. Outflow velocities versus log (N_H) for the different AGN types.
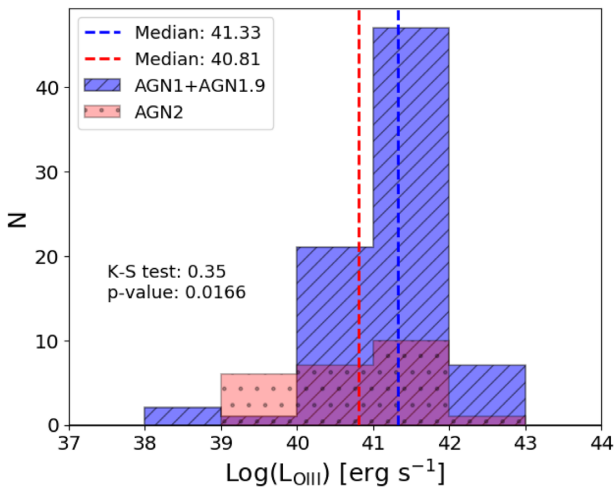

Figure 10. Luminosity distribution of the sources with an outflow detection. Type 1 + type 1.9 are in blue and type 2, in red. We consider here the narrow component of the [O III] line.

effectively corresponds to the transition from a population of type 1 AGNs with low N_H values to a population of type 1.9 AGNs with large N_H values.

5.3 Outflow fraction and luminosities

Fig. 10 shows the distribution of the AGN [O III] luminosities with an outflow detection for fixed bins of luminosity, where the [O III] luminosities correspond to the fitted narrow emission components, representing the AGNs. We can see that on average type 1 + type 1.9 are present at higher [O III] luminosities than type 2. This result is to be expected, since type 2 have typically lower luminosities, and [O III] scales with the X-ray luminosity.

Fig. 11 shows that the highest maximum velocities ($>1200\,\mathrm{km\,s^{-1}}$) are detected almost exclusively for [O III] luminosities higher than $10^{41}\,\mathrm{erg\,s^{-1}}$. This is in agreement with previous works where a slightly positive trend between the outflow velocity and the AGN luminosity was found (Reyes et al. 2008; Yuan, Strauss & Zakamska 2016; Fiore et al. 2017; Perna et al. 2017;
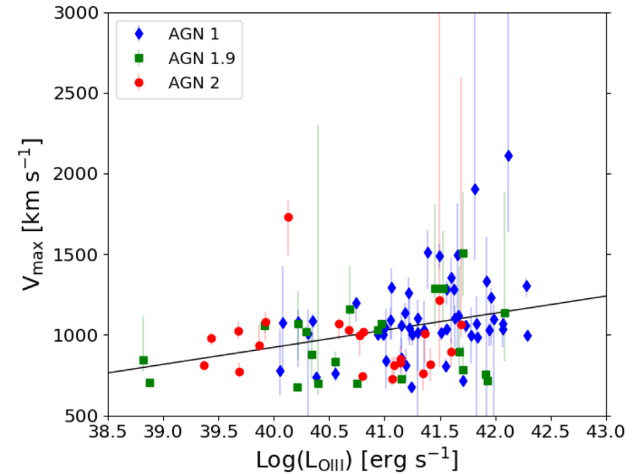
Figure 11. Outflow velocities as a function of log $L_{\mathrm{[O\,III]}}$ for the different AGN types. We consider here the narrow component of the [O III] line.

Rakshit & Woo 2018). However, there is no strong correlation between outflow velocity and [O III] luminosity. We use Spearman rank and Pearson test to quantify a possible correlation. The correlation coefficients are 0.3 and 0.1, with probabilities of <0.001 for the correlation being observed by chance, respectively. Perna et al. (2017) find a positive trend, although we note that this result included AGNs with low-velocity kinematics ($v_{\mathrm{max}} < 650\,\mathrm{km\,s^{-1}}$), which are excluded in our analysis. We also tested how the outflow velocity relates with bolometric luminosity and we found no correlation between both quantities, while e.g. Fiore et al. (2017) found a positive trend. However, we note that we cover a smaller range of luminosities than Fiore et al. (2017), between $\sim 10^{44}$–10^{46} and $\sim 10^{43}$–$10^{48}\,\mathrm{erg\,s^{-1}}$.

On the other hand, when we compare in Fig. 12 the fraction of outflows to $L_{\mathrm{[O\,III]}}$ and L_{Bol}, we note that type 1 + type 1.9 show about 20 per cent larger outflow fraction than type 2 for the different ranges of luminosities, and with little to no dependence on AGN luminosity for either type 1 + type 1.9 or type 2 AGNs.

Fig. 13 shows the estimated v_{max} as a function of L_{Bol}. We compare our findings with ionized outflows of obscured X-ray-selected quasars (Perna et al. 2015a; Brusa et al. 2016), [O III]-loud quasars at $z \sim 1.5$–2.5 with $L_{\mathrm{Bol}} > 10^{47}\,\mathrm{erg\,s^{-1}}$ (Carniani et al. 2015); massive AGNs at $z \sim 2$ (Genzel et al. 2014); low- and high-z (mostly type 2) AGNs (Harrison et al. 2012, 2014); and high-z radio-galaxies (Nesvadba et al. 2006, 2008). While when considering the BASS sample alone, no correlation is detected, the extension of the sample to larger AGN luminosities seems to imply mild positive correlation between maximum outflow velocity and AGN luminosity, with the ionized outflows discovered in BASS covering low-to-moderate velocities at the low AGN luminosity end of the diagram and various literature samples covering moderate-to-high AGN luminosities. We caution anyhow that the various sample selections applied in literature might affect the result.

5.4 Trend with the accretion rate

When we compare the distribution of outflow detections with the accretion rate (λ_{Edd}), we find that type 1 AGNs with outflows have a higher Eddington ratio than type 2 AGNs with outflows (see Fig. 14, with fixed bins of λ_{Edd}). However, this is simply reflecting the
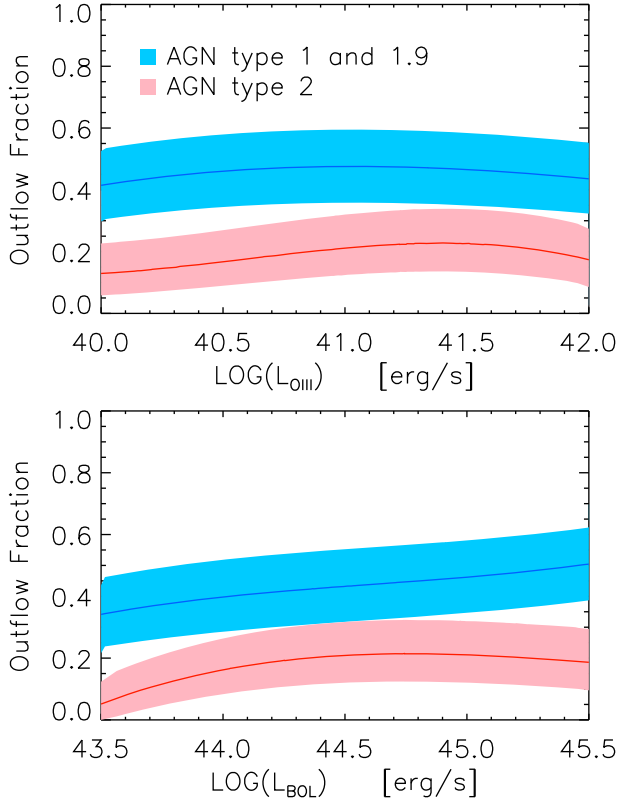
Figure 12. Outflow fraction as a function of luminosities log $L_{[O\,III]}$ and AGNs log L_{Bol} for the different AGN types. Fractions were obtained considering the sample of a fixed number of neighbouring objects in term of luminosity. Then, the resulting curve was then fitted with a low-order polynomial.

Eddington ratio difference found for the general population of type 1 and type 2 AGNs (e.g. Trump et al. 2011).

From Fig. 15, we can see that the outflow fraction in type 1 and type 1.9 AGNs is higher than in type 2 (~50 per cent versus 24 per cent). We can explain this difference with a couple of factors that can contribute: (a) type 2 AGNs include a population of highly obscured objects, where outflows have not yet managed to punch through the obscuring shell and drive the outflows; (b) type 2 AGNs, on average, will have higher covering factors of the obscuring material around them. Thus, even though they might have intrinsically high L_{BOL}, most of it will be reprocessed on small scales (i.e. most of the turbulent gas is contained within the torus), and only a smaller fraction of that energy will be deposited into ionizing and driving the outflows.

More intriguing is the fact that the outflow fraction appears to depend on the Eddington ratio: we see that the outflow fraction for type 2 AGN increases with λ_{Edd}, while the trend for type 1 and type 1.9 AGN seems to decrease or remain flat with accretion rates (see Fig. 15).

This behaviour is even clearer when we merge type 1 and type 1.9 AGNs together and compare their trend as a function of λ_{Edd} with respect to type 2 AGNs (see Fig. 16). While for the former there is no trend, the fraction of outflows in type 2 AGNs increases significantly (~3σ) above log (λ_{Edd}) $\gtrsim$ −1.5.

An interesting result to stress is shown in Fig. 17: In the upper panel, the behaviour between type 1 + type 1.9 and type 2 AGNs start to be significantly different at a given Eddington ratio, that is for log (λ_{Edd}) > − 1.7. This point is the same Eddington ratio where the
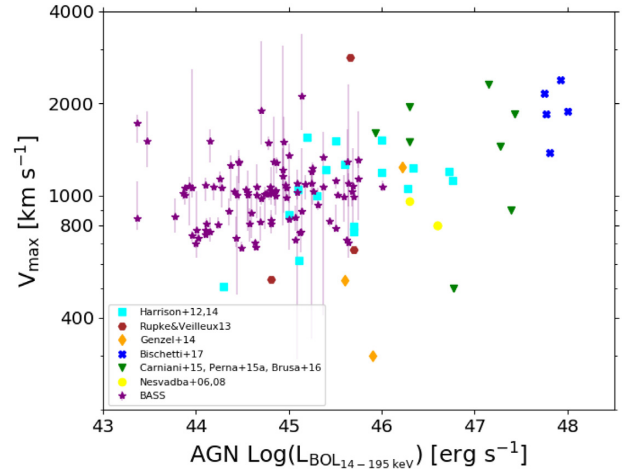

Figure 13. Maximum outflow velocities as a function of AGN log (L_{Bol}) compared with several literature samples (Nesvadba et al. 2006, 2008; Harrison et al. 2012, 2014; Rupke & Veilleux 2013; Genzel et al. 2014; Carniani et al. 2015; Perna et al. 2015a; Brusa et al. 2016; Bischetti et al. 2017).
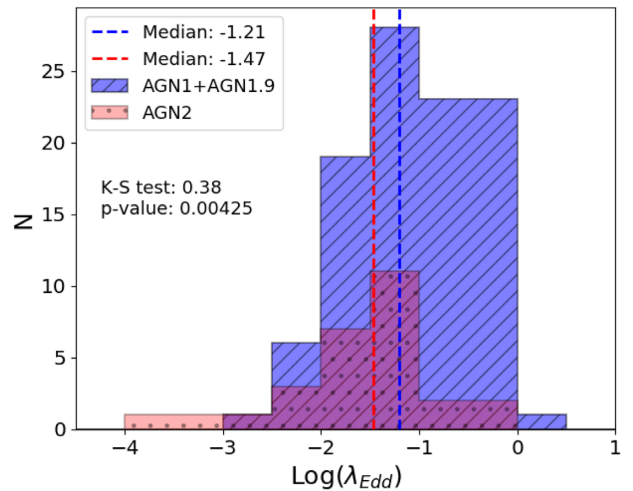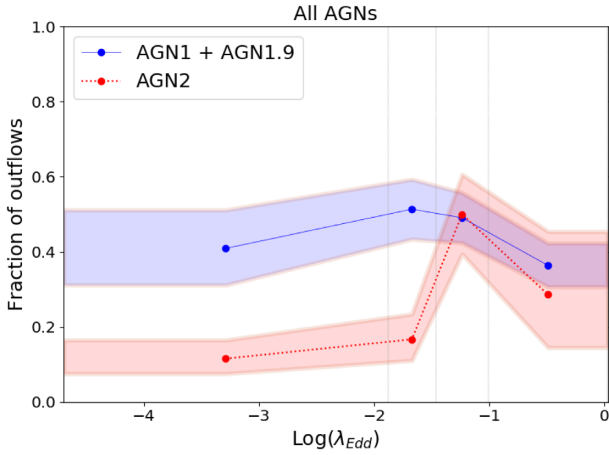

Figure 14. Distributions of Eddington ratio λ_{Edd} for broad-line (type 1 + type 1.9, dashed blue line) and narrow-line AGNs (type 2, dotted red line) with outflow detections. Broad-line AGNs have higher average λ_{Edd} values than narrow-line AGNs.

covering factor of obscured sources decreases significantly with the Eddington ratio according to Ricci et al. (2017b). In that scenario, this value can be interpreted as a threshold above which radiation pressure on dusty gas is able to create outflows (Fabian et al. 2016; Ishibashi et al. 2018). Then, when the Eddington ratio reaches the highest values ($\gtrsim$−1.2), most of the material around the BH has been blown away and winds cannot be sustained efficiently anymore. We compared our data with such interpretation, and can see that indeed the fraction of outflows increases for type 2 at log (λ_{Edd}) $\gtrsim$ −1.7 (see Fig. 17, bottom panel, red curve) to then drop at log (λ_{Edd}) $\gtrsim$ −0.8. Such drop can be understood as a selection effect: small covering factors mean it is very unlikely that these sources will be observed as type 2 AGNs. However, we do not see a similar trend for type 1 + type 1.9. In fact, puzzlingly, it seems that the outflow fraction in both type 1 + 1.9 and type 2
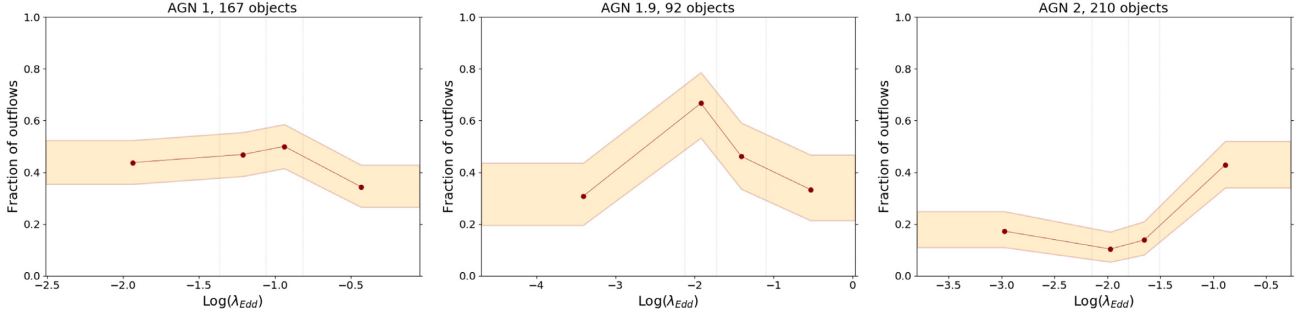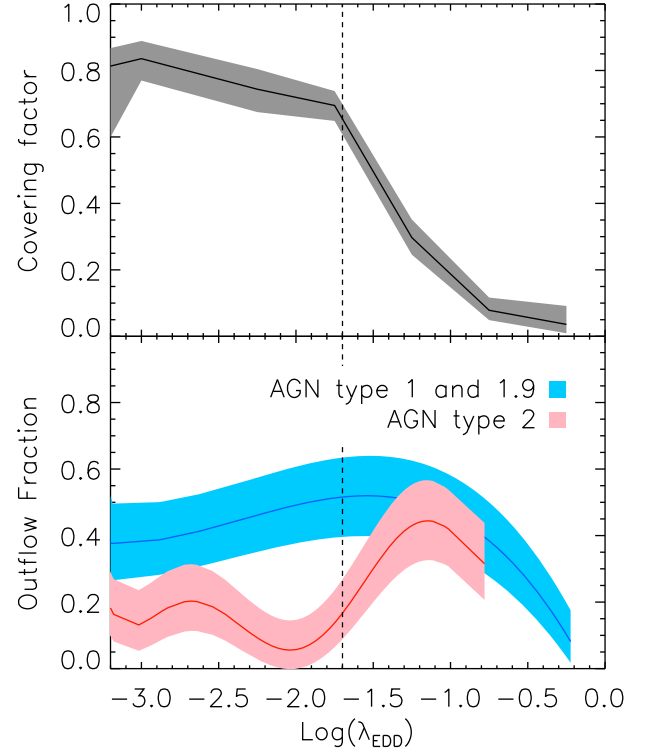
Figure 15. Fraction of detected outflows as a function of Eddington ratio λ_{Edd}, with each panel tracing the accretion rate trend for a given AGN type. Shaded areas represent the 16th and 84th quantiles of a binomial distribution, where bins are chosen to have the same number of objects and are indicated with vertical grey lines.

Figure 16. Fraction of outflows as a function of Eddington ratio λ_{Edd} comparing broad-line AGNs (AGN1 + AGN1.9; blue) and narrow-line AGNs (AGN2; red). Shaded areas represent the 16th and 84th quantiles of a binomial distribution, where bins are chosen to have the same number of objects and are indicated with grey vertical lines. Broad-line AGNs have a high and relatively flat fraction of outflow detected at different λ_{Edd}, while AGN2 have a very low detection fraction at low λ_{Edd} but increase dramatically to similar values as broad-line AGNs around $\log(\lambda_{Edd}) \gtrsim -1.5$.

Figure 17. Top panel: Fraction of obscured sources as in Ricci et al. (2017b) as a function of Eddington ratio for the BASS sample. Bottom panel: Outflow fraction of type 1 + type 1.9 (blue) and type 2 AGNs (red) as a function of λ_{Edd}. These fractions were obtained considering the sample of a fixed number of neighbouring objects in term of Eddington ratio. The resulting curves (blue and red) were then fitted with a low-order polynomial.

AGN starts to decrease above Eddington ratios of $\log(\lambda_{Edd}) \gtrsim -1.2$. At high $\log(\lambda_{Edd})$, the covering fraction of the obscuring material is rather low, as it can be seen in the upper panel. Thus, in type 2 AGNs the rise of outflow fraction happening at $\lesssim -1.7 \log(\lambda_{Edd}) \lesssim -0.8$ can be interpreted as the condition at which the obscuring material surrounding the engine, starts to blow out. Such effect is not visible in type 1 AGNs because they are not characterized by high covering factors. This is confirmed by the fact that above $\log(\lambda_{Edd}) \sim -1.0$ the blue (type 1 AGNs) and red (type 2 AGNs) curves in the bottom panel of Fig. 17 are again consistent, i.e. once the Eddington ratio becomes such that outflows cannot be sustained anymore. Our interpretation is supported by a Fisher's exact test to calculate the *p*-value significance of the difference in the two samples proportions as defined by the Eddington ratio of $\log(\lambda_{Edd}) = -1.7$. When comparing the outflows fractions for type 1 + type 1.9 and type 2 AGNs we obtained *p*-value = 0.001 for low $\log(\lambda_{Edd})$ and *p*-value = 0.12 for high $\log(\lambda_{Edd})$.

5.5 Outflow kinematics

In order to quantify the impact of these ionized outflows on the host galaxy, we need to determine their spatial extension and energetic. In this section, we calculate the mass outflow rate $[\dot{M}_{out} \, (\mathrm{M_\odot \, yr^{-1}})]$ and the kinetic power $[\dot{E}_{kin} \, (\mathrm{erg \, s^{-1}})]$ of the ionized outflows in our sample.

Considering the simple model of a spherically/biconically symmetric mass-conserving free wind, we can estimate the outflowing ionized gas mass, $\dot{M}_{out}$, from the fluid field continuity equation, assuming that most of the oxygen consists of O^{2+} ions with a gas

temperature of $T = 10^4$ K (typical temperature measured for the NLR), as in Carniani et al. (2015).

If the mean density of an outflow covering the solid angle $\Omega\pi$ is given by $\rho = \frac{3M_{ion}^{out}}{\Omega\pi R^3}$, then $\dot{M}_{out}$ can be estimated locally at a given radius r (e.g. Feruglio et al. 2015) by

$$\dot{M}_{out} = \Omega\pi r^2 \rho v = 3\frac{M_{ion}^{out}v}{r}, \qquad (4)$$

where v is v_{max}, given by equation (2) (assumed constant with radius and spherically symmetric in this simple bi-conical model) and M_{ion}^{out} is the ionized outflowing gas mass given by

$$M_{ion}^{out} = 4.0 \times 10^7\,M_{\odot} \left(\frac{C}{10^{[O/H]}}\right) \left(\frac{L_{[O\,III]}}{10^{44}\,erg\,s^{-1}}\right) \left(\frac{<n_e>}{10^3\,cm^{-3}}\right)^{-1}, \qquad (5)$$

where $L_{[O\,III]}$ is the luminosity of the [O III] $\lambda5007$ line tracing the outflow (from the flux of the broad-line component), $C = <n_e>^2 / <n_e^2>$ and n_e is the electron density. We assume $C \sim 1$ based on the hypothesis that all the ionized gas clouds have the same density, and $\log([O/H]) \sim 0$ (solar metallicity). However, large uncertainties in n_e and r propagate to a large uncertainty in the ionized mass outflow rate estimate, up to an order of magnitude. Indeed, the measured gas density n_e varies from a few hundreds up to several thousands of cm^{-3} for different methods in different samples (Cano-Díaz et al. 2012; Harrison et al. 2014; Carniani et al. 2015; Perna et al. 2015a, b; Kakkad et al. 2016; Bischetti et al. 2017; Fiore et al. 2017; Kakkad et al. 2018; Baron & Netzer 2019). In addition, we do not know the physical extent of our outflows because we are limited by single-slit spectroscopic observations with no spatial information.

Therefore, in order to limit the effects of such uncertainties, we use the correlation between the outflow size r (R_{out}) and the luminosity ($L_{[O\,III]}$) recently found by Kang & Woo (2018) to estimate R_{out}:

$$\log(R_{out}) = 0.28 \times \log(L_{[O\,III]}) - 11.34. \qquad (6)$$

To estimate the electron density we refer to Baron & Netzer (2019), where the authors use optical line ratios of [O III]/Hβ and [N II]/Hα, and the location of the wind estimated from mid-infrared emission. They found a value of $n_e \sim 10^{4.5}$ cm^{-3}, suggesting that the [S II]-based method commonly used by several authors, underestimates the true electron density in the outflowing gas by roughly 2 orders of magnitude.

Then, we derive the kinetic power associated with the outflow from the mass outflow rate by

$$\dot{E}_{kin} = \frac{1}{2}\dot{M}_{out}v^2. \qquad (7)$$

We estimate the wind momentum load as

$$w = \frac{\dot{P}_{out}}{\dot{P}_{AGN}} = \frac{\dot{M}_{out}v}{L_{Bol}/c}, \qquad (8)$$

where $\dot{M}_{out}v$ is the outflow momentum rate, and L_{Bol}/c is the AGN radiation pressure momentum. If $w < 10$, outflows are considered momentum-conserving, i.e. while expanding the gas decreases in temperature and releases energy through radiation. If w is larger, the outflows are considered energy-conserving, i.e. they expand adiabatically with constant temperature (see Zubovas & Nayakshin 2014 for details).

The estimated values of the mass outflow rate and kinetic energy as a function of L_{Bol} (as estimated from the hard X-ray luminosity) for our sample are presented in Figs 18 and 19. We find that the
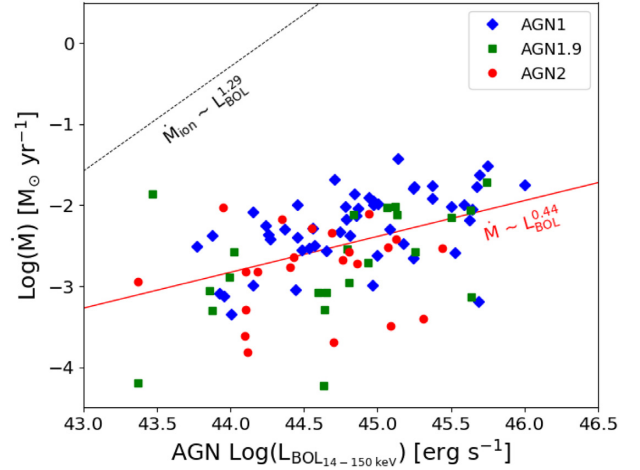
Figure 18. Mass outflow rate of the ionized outflows as a function of L_{Bol}. Dotted black line corresponds to the best-fitting relation derived for ionized outflows of Fiore et al. (2017), and solid red line corresponds to our best fit.
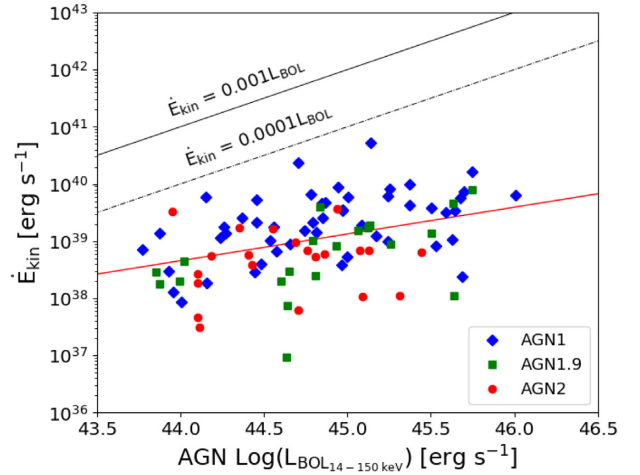
Figure 19. Kinetic power of the ionized outflows as a function of L_{Bol}. Dot–dashed and solid lines represent an outflow kinetic power that is 0.1 per cent and 0.01 per cent of the AGN bolometric luminosity, respectively.

energetics of the gas outflows are mildly correlated with bolometric luminosity. We use the Spearman rank and Pearson correlation test to derive the significance of the observed trends: we find coefficients of 0.46 and 0.20, with probabilities of <0.001 that the correlation is observed by chance. According to Fig. 18, ionized outflows at higher luminosities appear to expel a larger amount of the total ionized outflowing gas than outflows at lower luminosities. In addition, we note that they lie below the correlation found for ionized winds by Fiore et al. (2017), where the correlation between $\dot{M}$ and L_{Bol} has a log linear slope of 1.29 ± 0.38; instead, we find a slope of 0.44. This could be due to a different ionization density and spatial extension of the outflow region. The correlation of our data set is not as steep as Fiore et al. (2017). One explanation may be the different luminosity range covered by the BASS sample. Our sources are fainter than the sample presented in Fiore et al. (2017), and the onset of the correlation between outflow energetics and AGN bolometric luminosity could happen at higher luminosities.

Fig. 19 shows that the average kinetic power of our sample is less than 0.0001 per cent L_{Bol}, indicating very low energy conversion efficiencies, which are lower than some results in the literature. One

explanation here may be the different values assumed for the gas properties to estimate the kinetic power. For example, Rakshit & Woo ([2018](#)) found that their sample has on average ∼0.001 per cent L_{Bol}, assuming an electron density of $n_{\mathrm{e}} = 272$ cm^{-3}, while we used $n_{\mathrm{e}} = 10^{4.5}$ cm^{-3}. However, we found that our values of mass outflow rate and kinetic energy are in agreement with authors using higher values of electron density (e.g. Baron & Netzer [2019](#)). This reinforce the fact that using different assumptions in geometry and intrinsic properties of the wind leads important differences when we estimate their mass and kinematic power.

On the other hand, we estimate low wind-momentum loads for all AGN types, <0.1, in agreement with Fiore et al. ([2017](#)) where the range is estimated to be between 0.01 and 30. This suggests that the BASS AGN winds are probably momentum-conserving, as predicted by the King ([2003](#)) model.

Finally, we would like to stress that we used the $L_{\mathrm{[O\,III]}}$ of the outflow component to estimate $\dot{M}_{\mathrm{out}}$ and $\dot{E}_{\mathrm{kin}}$, so we do not expect to the perceived correlations showed in Figs [18](#) and [19](#) are due to a trend between $L_{\mathrm{[O\,III]}}$ and L_{Bol}. Moreover, the total $L_{\mathrm{[O\,III]}}$ and bolometric luminosity quantities are found to be not correlated, with a huge scatter between $L_{\mathrm{[O\,III]}}$ and X-ray (∼L_{Bol}) emission (see e.g. Berney et al. [2015](#); Ueda et al. [2015](#)).

6 SUMMARY AND CONCLUSIONS

The aim of this work is to test the incidence of ionized outflows for a large sample of nearby hard X-ray-selected AGNs, and to study how the outflow properties are related to different AGN tracers (X-ray, [O III], and bolometric luminosities, M_{BH}, λ_{Edd}).

The modelling of the optical spectra of hard X-ray-selected AGNs allowed us to derive the incidence and properties of ionized outflows in an unbiased/complete sample covering a wide range of AGN bolometric luminosities, and to study the differences between obscured and unobscured AGNs.

According to this, to investigate the presence of an outflow, we focus on the [O III] λλ4959, 5007 emission lines. In particular, we used a multicomponent fitting procedure to account for the faint wings of [O III] associated with an outflow signature. Outflow velocities were estimated using two different approaches: following the criteria of Rupke & Veilleux ([2013](#)) who use the parameters of both fitted components of the line, and a non-parametric method that is expected to be less sensitive at low S/N.

We found that 38 ± 2 per cent of our AGN sample analysed (178/469) present detected outflows, mostly blueshifted, and that the fraction of blue versus redshifted outflows in our sample is consistent with a simple geometrical unification of Type 1/type 2 AGNs.

We test how the outflow fraction and velocities relate to the AGN properties. We observe an increasing outflows fraction as a function of Eddington ratio for type 2 AGNs, and we find weak trends between outflow velocity and AGN luminosity (as traced by L_{X}, $L_{\mathrm{O\,iii}}$, or L_{Bol}), and no evident trend between outflow incidence and X-ray obscuration. The Eddington ratio seems to be a fundamental parameter to understand the type 1 versus type 2 AGN dichotomy from the point of view of outflow frequency.

Finally, we estimate the kinetic energy and power of the outflows, adopting several assumptions about the physical geometry and gas conditions. An important caveat to bear in mind is that we are only able to trace the ionized phase of the outflows, and we must factor in the neutral and molecular components (which will require additional observations), in order to put constraints on the overall mechanics governing outflows in these sources.

REFERENCES

Alexander D. M., Hickox R. C., 2012, New Astron. Rev., 56, 93
Antonucci R., 1993, ARA&A, 31, 473
Balmaverde B. et al., 2016, A&A, 585, A148
Bär R. E. et al., 2019, MNRAS, 489, 3073
Baek J. et al., 2019, MNRAS, 488, 4317
Baron D., Netzer H., 2019, MNRAS, 486, 4290
Baumgartner W. H., Tueller J., Markwardt C. B., Skinner G. K., Barthelmy S., Mushotzky R. F., Evans P. A., Gehrels N., 2013, ApJS, 207, 19
Berney S. et al., 2015, MNRAS, 454, 3622
Bischetti M. et al., 2017, A&A, 598, A122
Boroson T. A., Green R. F., 1992, ApJS, 80, 109
Brusa M. et al., 2016, A&A, 588, A58
Cano-Díaz M., Maiolino R., Marconi A., Netzer H., Shemmer O., Cresci G., 2012, A&A, 537, L8
Cappellari M., Emsellem E., 2004, PASP, 116, 138
Carniani S. et al., 2015, A&A, 580, A102
Carniani S. et al., 2016, A&A, 591, A28
Cicone C. et al., 2014, A&A, 562, A21
Cresci G. et al., 2015, ApJ, 799, 82
Di Matteo T., Springel V., Hernquist L., 2005, Nature, 433, 604
Dimitrijević M. S., Popović L. Č., Kovačević J., Dačić M., Ilić D., 2007, MNRAS, 374, 1181
Fabian A. C., 2012, ARA&A, 50, 455
Fabian A. C. et al., 2016, MNRAS, 461, 922
Ferland G. J. et al., 2013, Rev. Mex. Astron. Astrofis., 49, 137
Ferrarese L., Merritt D., 2000, ApJ, 539, L9
Feruglio C., Maiolino R., Piconcelli E., Menci N., Aussel H., Lamastra A., Fiore F., 2010, A&A, 518, L155
Feruglio C. et al., 2015, A&A, 583, A99
Fiore F. et al., 2017, A&A, 601, A143
Fischer T. C., Crenshaw D. M., Kraemer S. B., Schmitt H. R., 2013, ApJS, 209, 1
Gebhardt K. et al., 2000, ApJ, 539, L13
Gehrels N. et al., 2004, ApJ, 611, 1005
Genzel R. et al., 2014, ApJ, 796, 7
Ginsburg A., Mirocha J., 2011, Astrophysics Source Code Library, record ascl:1109.001
Granato G. L., De Zotti G., Silva L., Bressan A., Danese L., 2004, ApJ, 600, 580
Harrison C. M. et al., 2012, MNRAS, 426, 1073
Harrison C. M., Alexander D. M., Mullaney J. R., Swinbank A. M., 2014, MNRAS, 441, 3306

Harrison C. M. et al., 2016, MNRAS, 456, 1195

Hernández-García L., Masegosa J., González-Martín O., Márquez I., Guainazzi M., Panessa F., 2017, A&A, 602, A65

Hirschmann M., Khochfar S., Burkert A., Naab T., Genel S., Somerville R. S., 2010, MNRAS, 407, 1016

Hopkins P. F., Hernquist L., Cox T. J., Di Matteo T., Robertson B., Springel V., 2006, ApJS, 163, 1

Hopkins P. F., Hernquist L., Cox T. J., Kereš D., 2008, ApJS, 175, 356

Ichikawa K. et al., 2019, ApJ, 870, 31

Ishibashi W., Fabian A. C., 2012, MNRAS, 427, 2998

Ishibashi W., Fabian A. C., Maiolino R., 2018, MNRAS, 476, 512

Jahnke K., Macciò A. V., 2011, ApJ, 734, 92

Kakkad D. et al., 2016, A&A, 592, A148

Kakkad D. et al., 2018, A&A, 618, A6

Kang D., Woo J.-H., 2018, ApJ, 864, 124

King A., 2003, ApJ, 596, L27

Kormendy J., Ho L. C., 2013, ARA&A, 51, 511

Koss M. et al., 2017, ApJ, 850, 74

Koss M. J. et al., 2018, Nature, 563, 214

Lamperti I. et al., 2017, MNRAS, 467, 540

Maiolino R. et al., 2017, Nature, 544, 202

Masetti N. et al., 2013, A&A, 556, A120

Merloni A., Heinz S., 2008, MNRAS, 388, 1011

Nesvadba N. P. H., Lehnert M. D., Eisenhauer F., Gilbert A., Tecza M., Abuter R., 2006, ApJ, 650, 693

Nesvadba N. P. H., Lehnert M. D., De Breuck C., Gilbert A. M., van Breugel W., 2008, A&A, 491, 407

Oh K. et al., 2017, MNRAS, 464, 1466

Oh K. et al., 2018, ApJS, 235, 4

Paliya V. S. et al., 2019, ApJ, 881, 154

Peng C. Y., 2007, ApJ, 671, 1098

Perna M. et al., 2015a, A&A, 574, A82

Perna M. et al., 2015b, A&A, 583, A72

Perna M., Lanzuisi G., Brusa M., Mignoli M., Cresci G., 2017, A&A, 603, A99

Peterson B. M., 1997, An Introduction to Active Galactic Nuclei. Cambridge Univ. Press, Cambridge/New York, p. 238

Pogge R. W., 1989, ApJS, 71, 433

Powell M. C. et al., 2018, ApJ, 858, 110

Rakshit S., Woo J.-H., 2018, ApJ, 865, 5

Reyes R. et al., 2008, AJ, 136, 2373

Ricci C., Ueda Y., Koss M. J., Trakhtenbrot B., Bauer F. E., Gandhi P., 2015, ApJ, 815, L13

Ricci C. et al., 2017a, ApJS, 233, 17

Ricci C. et al., 2017b, Nature, 549, 488

Ricci C. et al., 2018, MNRAS, 480, 1819

Rojas A. F. et al., 2017, A&A, 602, A124

Rupke D. S. N., Veilleux S., 2013, ApJ, 768, 75

Sani E., Marconi A., Hunt L. K., Risaliti G., 2011, MNRAS, 413, 1479

Shangguan J., Ho L. C., Xie Y., 2018, ApJ, 854, 158

Shen Y. et al., 2016, ApJ, 831, 7

Shimizu T. T. et al., 2018, ApJ, 856, 154

Storey P. J., Zeippen C. J., 2000, MNRAS, 312, 813

Trakhtenbrot B. et al., 2017, MNRAS, 470, 800

Trump J. R. et al., 2011, ApJ, 733, 60

Ueda Y. et al., 2015, ApJ, 815, 1

Urry C. M., Padovani P., 1995, PASP, 107, 803

Vazdekis A., Ricciardelli E., Cenarro A. J., Rivero-González J. G., Díaz-García L. A., Falcón-Barroso J., 2012, MNRAS, 424, 157

Veilleux S., 1991, ApJS, 75, 357

Véron-Cetty M.-P., Véron P., Gonçalves A. C., 2001, A&A, 372, 730

Vietri G. et al., 2018, A&A, 617, A81

Winkler H., 1992, MNRAS, 257, 677

Woo J.-H., Bae H.-J., Son D., Karouzos M., 2016, ApJ, 817, 108

Woo J.-H., Son D., Bae H.-J., 2017, ApJ, 839, 120

Yuan S., Strauss M. A., Zakamska N. L., 2016, MNRAS, 462, 1603

Zakamska N. L., Greene J. E., 2014, MNRAS, 442, 784

Zubovas K., Nayakshin S., 2014, MNRAS, 440, 2625

[1] *European Southern Observatory, Alonso de Cordova 3107, Casilla 19, Santiago 19001, Chile*

[2] *Departamento de Ciencias Fisicas, Universidad Andres Bello, Campus La Casona, Fernandez Concha 700, 7500912 Santiago, Chile*

[3] *Núcleo de Astronomía de la Facultad de Ingeniería, Universidad Diego Portales, Av. Ejército Libertador 441, 8320000 Santiago, Chile*

[4] *Kavli Institute for Astronomy and Astrophysics, Peking University, Beijing 100871, People's Republic of China*

[5] *Department of Physics and Astronomy, University College London, Gower Street, London WC1E 6BT, UK*

[6] *Eureka Scientific, Inc., 2452 Delmer Street Suite 100, Oakland, CA 94602-3017, USA*

[7] *School of Physics and Astronomy, Tel Aviv University, Tel Aviv 69978, Israel*

[8] *Institute for Particle Physics and Astrophysics, ETH Zürich, Wolfgang-Pauli-Strasse 27, CH-8093 Zürich, Switzerland*

[9] *Department of Astronomy, Kyoto University, Oiwake-cho, Sakyo-ku, Kyoto 606-8502, Japan*

[10] *Korea Astronomy & Space Science institute, 776, Daedeokdae-ro, Yuseong-gu, Daejeon 34055, Republic of Korea*

[11] *Instituto de Astrofísica, Facultad de Física, Pontificia Universidad Católica de Chile, Casilla 306, Santiago 22, Chile*

[12] *Millennium Institute of Astrophysics (MAS), Nuncio Monseñor Sótero Sanz 100, Providencia, 7500912 Santiago, Chile*

[13] *Space Science Institute, 4750 Walnut Street, Suite 205, Boulder, CO 80301, USA*

[14] *INAF – Osservatorio Astronomico di Roma, Via Frascati 33, I-00078 Monte Porzio Catone (Roma), Italy*

[15] *Massachusetts Institute of Technology, Kavli Institute for Astrophysics, Cambridge, MA 02139, USA*

[16] *Cahill Center for Astronomy and Astrophysics, California Institute of Technology, Pasadena, CA 91125, USA*

[17] *INAF – Osservatorio di Astrofisica e Scienza dello Spazio, via Gobetti 93/3, I-40129 Bologna, Italy*

[18] *Max-Planck-Institut für extraterrestrische Physik, Postfach 1312, D-85741 Garching, Germany*

[19] *Astronomical Observatory, Volgina 7, 11060 Belgrade, Serbia*

[20] *Sterrenkundig Observatorium, Universiteit Gent, Krijgslaan 281-S9, Gent B-9000, Belgium*

[21] *Jet Propulsion Laboratory, California Institute of Technology, 4800 Oak Grove Drive, MS 169-224, Pasadena, CA 91109, USA*

[22] *Cluster of Excellence, Boltzmann-Str 2, D-85748 Garching bei München, Germany*

[23] *European Southern Observatory, Karl Schwarzschild Str 2, D-85748 Garching, Germany*

[24] *INAF – Istituto di Astrofisica Spaziale e Fisica Cosmica Milano, Via Corti 12, I-20133 Milano, Italy*

This paper has been typeset from a TEX/LATEX file prepared by the author.